

Supporting Information for

Nanoconfinement Effects on Water in Narrow Graphene-based Slit Pores as Revealed by THz Spectroscopy

Sergi Ruiz-Barragan,^{*a,b} Federico Sebastiani,^{c,d} Philipp Schienbein,^{a,e} Jijo Abraham,^f
Gerhard Schwaab,^c Rahul R. Nair,^f Martina Havenith,^c and Dominik Marx^a

^a *Lehrstuhl für Theoretische Chemie, Ruhr-Universität Bochum,
44780 Bochum, Germany; E-mail: sergi.ruiz@theochem.rub.de*

^b *Present Address: Institute of Computational Chemistry and Catalysis (IQCC) and Departament de Química,
Universitat de Girona, Carrer Maria Aurèlia Capmany 69, 17003 Girona, Spain*

^c *Lehrstuhl für Physikalische Chemie II, Ruhr-Universität Bochum, 44780 Bochum, Germany*

^d *Present Address: Department of Chemistry "Ugo Schiff", University of Florence,
Via della Lastruccia 3-8, 50019 Sesto Fiorentino (FI), Italy*

^e *Present Address: Department of Physics and Astronomy and Thomas Young Centre,
University College London, London WC1E 6BT, United Kingdom*

^f *National Graphene Institute, Department of Chemical Engineering,
University of Manchester, Manchester M13 9PL, United Kingdom*

CONTENTS

I. Experimental Materials and Methods	S2
A. GO-Membranes: Materials	S2
B. THz Spectroscopy: Methods	S2
II. Computational Approaches and Simulation Details	S4
A. Slit Pore Models	S4
B. Simulation Details	S4
C. Water-Graphene Force Field for QM/MM Simulations	S5
D. Pressure Control	S7
1. Intrinsic Density Correction	S7
2. Rigid Piston Simulations: Validation	S8
3. Frozen Piston Simulations: Interlayer Distance Determination	S9
III. Dissection of Theoretical THz Spectra	S10
A. Polarization-resolved Spectra	S10
B. Cross-correlation Analysis	S10
C. Orientational Decomposition	S11
D. Layer-wise Decomposition	S12
IV. Supporting Computational Analyses	S13
A. Full-range IR spectra	S13
B. Vibrational Density of States (VDOS)	S14
C. Two-body Vibrational Density of States (2B-VDOS)	S15
D. M Slit Pore System: Spectral Decompositions	S15
References	S17

I. EXPERIMENTAL MATERIALS AND METHODS

A. GO-Membranes: Materials

The graphene-oxide membranes (GO-membranes), as described in the Main Text, were prepared as detailed in Ref. 1. Their microscopic structure is shown in Fig. S1, resulting from random stacking of GO crystallites consisting of pristine and oxidized region formed between graphene sheets. The amount of pristine graphene and graphene oxide was about 60 and 40 % of the membrane, respectively. Their complex network of interlayer, interedge spaces, and wrinkles allows water to percolate within the single sheets of these graphene-based membranes. The GO-membranes with 0.8 and 1.0 nm interlayer distances were obtained by swelling of vacuum-dried membranes under 33 and 100 % relative humidity, respectively, for one week. The GO-membrane with 1.4 nm interlayer distance was obtained by soaking the dry membrane in liquid water. For this latter sample, excess water on the surface of the membranes was removed before the measurements. The water content at each of the investigated interlayer distances was estimated with respect to the vacuum-dried membrane. The relative humidity level as well as the interlayer distance was kept constant during the measurements by using a vacuum-tight sample cell.

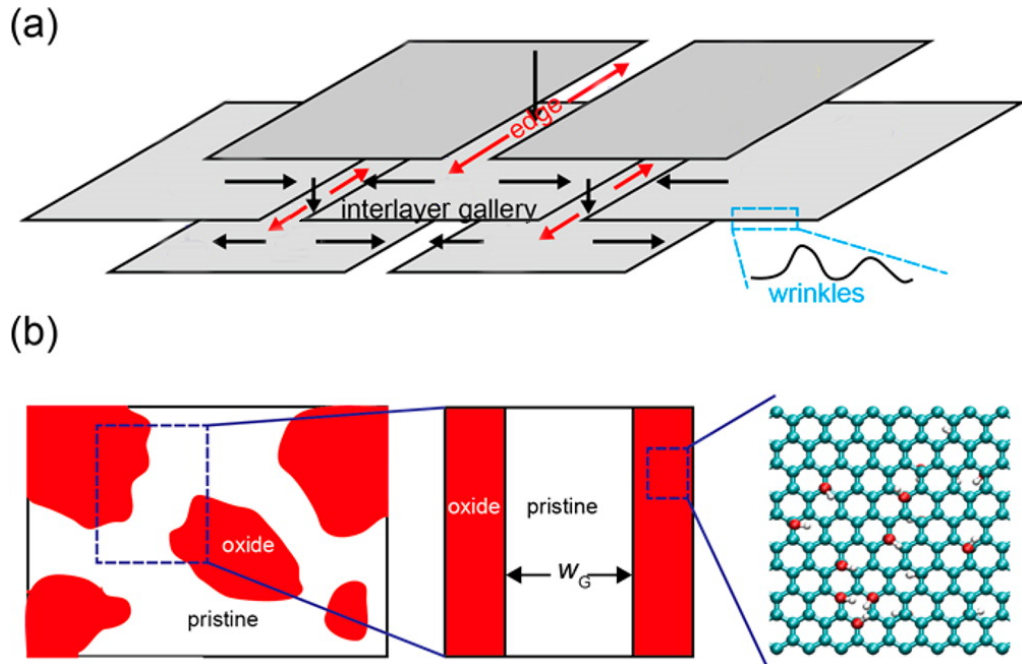


Figure S1. Microstructures of graphene-derived membranes. (a) The percolated water transport channel is composed of interlayer, interedge spaces, and wrinkles within the graphene sheets. (b) The pristine and oxidized patterns on GO (left) are modeled in a quasi-2D molecular model, where W_G is the pristine graphene channel width, (center) with oxygen-containing functionalization groups on both sides (right). Adapted from Ref. 2. Copyright 2014 American Chemical Society.

B. THz Spectroscopy: Methods

THz-Far Infrared (THz-FIR) absorption measurements have been performed by means of a Bruker Vertex 80v Fourier Transform InfraRed (FTIR) spectrometer equipped with a liquid helium cooled silicon bolometer from Infrared Laboratories as detector. A mercury arc lamp was used as light source of the broadband THz radiation, while a Mylar-multilayer beamsplitter was employed for the generation of the interferogram. The sample compartment was continuously purged with technical grade dry nitrogen to minimize air humidity. The data of the GO-membranes reported here were recorded using a vacuum-tight temperature-controlled sample cell at $20.0 \pm 0.2^\circ\text{C}$ and at a sample compartment humidity level below 5 %. For these measurements we used a Bruker liquid cell with chemical vapor deposition-grown diamond windows (Diamond Materials, GmbH). The GO-membranes were placed between the diamond windows of the cell and were measured in transmission geometry in the frequency range from 30 to 650 cm^{-1} as an average over 128 scans with a resolution of 2 cm^{-1} . The spectra were smoothed with a 3 cm^{-1} wide (7 points) moving average. The frequency-dependent absorbance of the GO-membranes, $A(\nu)$, is expressed as

$$A(\nu) = \log_{10} \left(\frac{I_{\text{BG}}(\nu)}{I_{\text{GO-membrane}}(\nu)} \right) \quad (1.1)$$

where $I_{\text{BG}}(\nu)$ and $I_{\text{GO-membrane}}(\nu)$ are the transmitted intensities of the empty instrument and the GO-membrane at room temperature, respectively. The residual absorption due to the air water vapour in the beam path was corrected by subtracting a scaled spectrum of water vapor.

To analyze only the signal arising from the water confined in the GO-membranes, we took the difference absorbance spectra for wet GO-membranes (i.e. at respective interlayer distances of 0.8, 1.0 and 1.4 nm) to the spectra of the corresponding dry GO-membranes

$$\Delta A = A_{\text{wet GO-membrane}}(\nu) - A_{\text{dry GO-membrane}}(\nu) \quad (1.2)$$

These spectra ΔA have been normalized to the intensity of the band at about 200 cm^{-1} of the water in GO-membrane system at 1.4 nm.

As routinely done in THz-FIR absorption data analysis (see for example Refs. 3, 4), the differential absorbance spectra from 30 to 650 cm^{-1} were fitted with Wolfram Mathematica to a sum of damped harmonic oscillator functions

$$\sum_{n=1}^N \mathcal{L}_n = \sum_{n=1}^N \frac{a_n w_n^2 \nu^2}{4\pi^3 \left[\frac{\nu^2 w_n^2}{\pi^2} + \left(\nu_{d,n}^2 + \frac{w_n^2}{4\pi^2} - \nu^2 \right)^2 \right]} \quad (1.3)$$

with a_n , w_n , and $\nu_{d,n}$ describing the amplitude, the width and the perturbed center frequency of the n -th mode, respectively. The unperturbed center frequency (ν_n) can then be deduced accordingly

$$\nu_n = \sqrt{\nu_{d,n}^2 + \frac{w_n^2}{4\pi^2}}. \quad (1.4)$$

The linewidths of the resonances have been fixed in the final fitting procedure after a first fit run, where all the fitting parameters were kept free. The results of these fits are reported in the Main Text in Table 1 and Fig. 6.

In Fig. S2, we plot the relative intensity of the bands used to dissect the intermolecular stretching band around 200 cm^{-1} for the GO-membranes with interlayer distances corresponding to $d_{\text{int}} = 0.8, 1.0$ and 1.4 nm . Upon

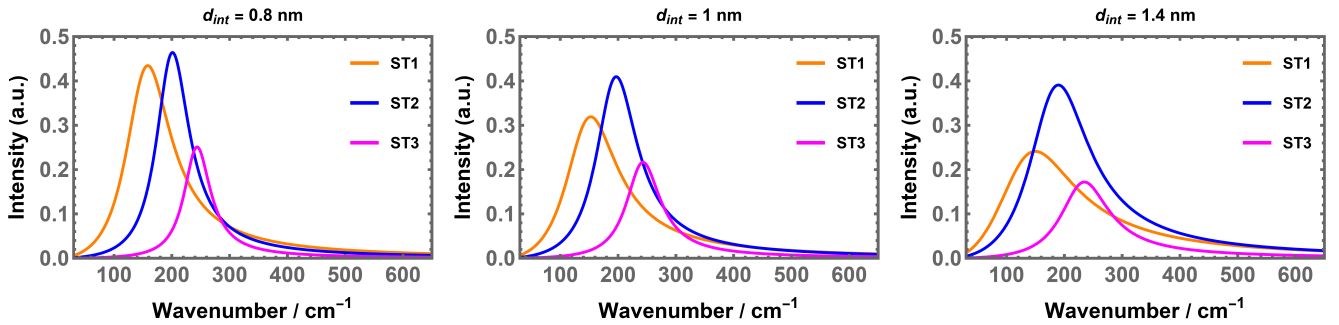


Figure S2. Relative intensities of the ST1 (orange line), ST2 (blue line) and ST3 (magenta line) modes describing the intermolecular stretching band around 200 cm^{-1} of the experimental spectra of water confined in GO-membranes at $d_{\text{int}} = 0.8, 1.0$ and 1.4 nm from left to right, respectively.

increasing the interlayer distance d_{int} from 0.8 to 1.4 nm, ST1 and ST3 shift under the ST2 band, become broad and their intensities decrease, as in multilamellae systems the contributions of the H-bonds within each water layer and of the H-bonds directly interconnecting the interfacial water layers, are less defined and contribute less to the total absorption profile. On the contrary, ST2 becomes the major component at the largest investigated interlayer distance, i.e. as increasing the total water content in the GO-membranes (see Main Text for details).

II. COMPUTATIONAL APPROACHES AND SIMULATION DETAILS

A. Slit Pore Models

The four slit pore models used to compute, decompose and assign THz spectra of nanoconfined water herein are denoted as extra small (XS), small (S), medium (M) and large (L) systems and consist of two periodically extended graphene walls (being parallel coplanar graphene sheets at a fixed interlayer distance determined as explained below) which host water lamellae with a number of water molecules as specified in Table S1. Representative snapshots of all systems as obtained from microcanonical (NVE) simulations performed to calculate the IR spectra from far-IR (THz) up to mid-IR frequencies are depicted in Figure S3. The graphene sheets contain 112 carbon atoms each, providing lattice constants of $a = 17.12 \text{ \AA}$ and $b = 17.30 \text{ \AA}$ which span the xy plane. Transcending our earlier work on such systems [5], the interlayer distance between the two graphene walls (see d_{int} in Table S1) has been determined for each system at 300 K by applying a nominal normal pressure of 1 bar using the frozen piston approach together with the intrinsic density correction (explained in Section IID) as introduced recently [6]. A vacuum space of 15 \AA has been added perpendicular to the graphene layers (z -direction) to decouple the periodic supercells normal to the confining walls.

Table S1. Structural parameters and number of H_2O molecules ($N_{\text{H}_2\text{O}}$) for each of the studied systems with in-plane (xy) lattice constants of $a = 17.12 \text{ \AA}$ and $b = 17.30 \text{ \AA}$ and the perpendicular (z) supercell constant $c = L_z$. The fixed interlayer distances between the graphene walls (d_{int}) have been determined for each slit pore setup from corresponding rigid piston simulations as detailed in Section IID and used in the production simulations using the frozen piston approach.

System	XS	S	M	L
$N_{\text{H}_2\text{O}}$	27	54	80	105
L_z (\AA)	21.68	29.41	27.26	29.69
d_{int} (\AA)	6.68	9.41	12.26	14.69

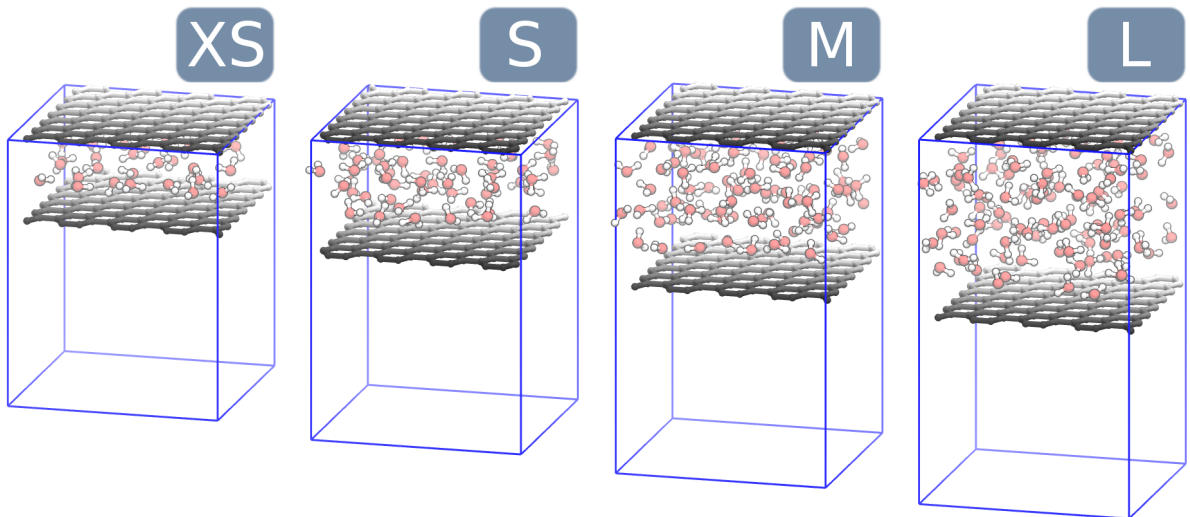


Figure S3. Representative configuration snapshots of all four slit pores, XS to L from left to right, using frozen graphene walls with an interlayer distance d_{int} as optimized using corresponding rigid piston NVE simulations; see Section IID for background and details.

B. Simulation Details

All simulations were performed with CP2K [7–10]. A QM/MM approach [11] is used in all (NVT and NVE, see below) simulations to reduce the computational effort in view of the significant statistics required to compute converged IR lineshapes down to THz frequencies. All water molecules are included in the QM system whereas the two graphene layers constitute the MM system. The water–graphene interactions that couple the QM and MM systems are described using two Lennard-Jones (LJ) potentials for which the parameters have been optimized in this work to reproduce our previous (all-QM RPBE-D3) water densities within very similar slit pore setups [5]. The optimization procedure is described later in Section IIC and the values are reported in Table S2. All water molecules are described using the RPBE density functional [12] supplemented with the D3 dispersion correction considering as usual only the two-body terms and applying zero damping [13]. We used GTH pseudopotentials [14–16] and a triple- ζ plus double polarization

Gaussian basis set, TZV2P, setting the density cutoff for the auxiliary plane wave basis set to 500 Ry. For the rigid piston approach simulations used to determine the interlayer distance, see Section IID, we use a full QM description for all atoms, i.e. RPBE-D3. Note that this electronic-structure-based description of water-graphene interfaces has been carefully validated by us previously (see Section I.B in the SI of Ref. 5) and confirmed later by others based on much more extensive benchmarks [17] (see in particular the “water@graphene” GGA data in Figure 2 therein).

The IR/THz absorption spectra are calculated using the Fourier transform of the dipole time autocorrelation function [18, 19] as detailed below. As usual, the effective dipole moments of the individual water molecules are computed within ab initio molecular dynamics AIMD [11] simulations (or within the QM subsystem of QM/MM simulations as done in the present case) using the centers of maximally localized Wannier functions to include many-body electronic polarization and charge transfer effects (see e.g. Ref. 11 for background and methods). To avoid any perturbation from the thermostating implied in all canonical (NVT) simulations, these respective time correlation functions are calculated using 60 independent NVE trajectories of 20 ps length each for every slit pore setup, the average of which provides the reported spectra and properties. To obtain the initial conditions (positions and velocities) for each NVE simulation, a previous NVT simulation of 60 ps duration was performed for each system at 300 K subject to Nosé-Hoover-chain thermostating. Initial conditions were sampled every 2.5 ps and used to launch independent NVE simulations. The timestep of the NVT and NVE simulations was 0.4 fs whereas the Wannier centers have been computed and stored for analyses every 0.8 fs. Using this scheme, the NVT ensemble is properly sampled after averaging the properties using all NVE simulations, notably including time dependent properties such as the dipole time-autocorrelation functions in the present case, at the desired average temperature which is close to 300 K. In these frozen piston QM/MM simulations of the slit pores, a perpendicular pressure of 1 bar has been established using our rigid piston approach as explained in Section IID 2 by determining the proper interlayer distances d_{int} together with applying the determined excess pressure of 1.6 kbar to correct the intrinsic water density of the RPBE-D3 model to reproduce the experimental density at 1 bar (and 300 K) according to Section IID 1. For the bulk simulations, the water density has been fixed at the experimental value [20] at 1 bar and 300 K via the volume of the periodic cubic supercell filled with 128 water molecules.

C. Water-Graphene Force Field for QM/MM Simulations

As shown previously, properties of nanoconfined water in narrow slit pores can be faithfully described using LJ interactions between water and graphene [5, 6]. In view of the enormous statistics that is required to converge THz spectra, see above, we introduce here a hybrid methodology. Specifically, we employ a QM/MM MD scheme where the carbon atoms act as LJ centers for the oxygen and hydrogen atoms of water (denoted by LJ+RPBE-D3). Note that all carbon atoms are frozen in space for the production simulations in view of using the frozen piston approach described in the following section.

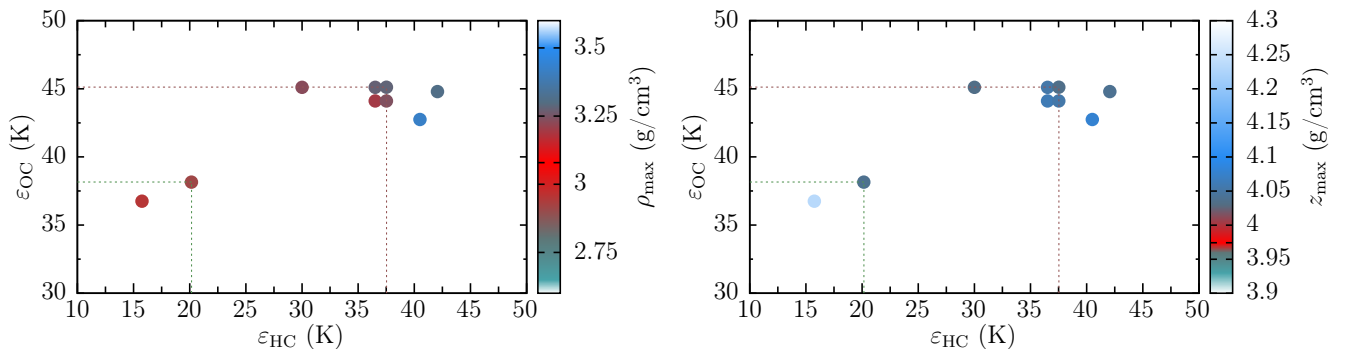


Figure S4. (a) Water density at the peak maximum corresponding to the first solvation shell of graphene (in g/cm^3) for different combinations of ϵ_{OC} and ϵ_{HC} for the slit pore system L from our previous work [6] (see text for details) and (b) corresponding position (in \AA) of that maximum with respect to $z = 0 \text{ \AA}$ in that frozen piston slit pore setup as encoded by the color bars on the right axes. The marked points are the LJ-L and the last guess for the LJ-QM/MM parameter sets using the interpolation scheme (see text for details). Red color corresponds to the same value as full QM simulation ($\rho_{\text{max}} = 3.08 \text{ g}/\text{cm}^3$, $z_{\text{max}} = 3.97 \text{ \AA}$). Note that the axes labeling in this figure has been corrected on 2023/12/20.

To be consistent with our previous studies of nanoconfined water in graphene slit pores [5, 6], the LJ parameters ($\sigma_{\text{OC}}, \epsilon_{\text{OC}}; \sigma_{\text{HC}}, \epsilon_{\text{HC}}$) have been optimized to reproduce the density profiles as obtained from corresponding all-QM RPBE-D3 simulations of all systems; recall that the RPBE-D3 density functional has been carefully validated previously by us and others [5, 17]. We used the interpolation scheme as established for all-MM simulations in our previous work [6], thus determining now the water density profiles for different combinations of ϵ_{OC} and ϵ_{HC} parameters while using QM/MM simulations and analyzing the height (ρ_{max}) as well as the position (z_{max}) of the

first density maximum perpendicular to graphene. However, as the QM/MM simulations are much more expensive than the previous all-MM (force field molecular dynamics) simulations, first we started with only four points with our previous L slit pore (14.41Å). We take these so-called LJ-L parameters (optimized previously for “large” slit pore widths and SPC/E force field water [6], see Table S2), as starting point and varied slightly the ε_{OC} and ε_{HC} parameters to obtain four sets of LJ parameters. With these sets, a 100 ps QM/MM simulation is performed for each set and the height of the first maximum of the density is analyzed for every simulation. Using these four values, our previous fitting scheme [6] can be used to determine the best set of LJ parameters. However, as only four data points are employed, the new set is extrapolated (instead of interpolated) and when we performed a new 100 ps QM/MM simulation with these parameters, the ρ_{max} is far from the QM/MM reference. For that reason, this new height is again introduced in the fitting scheme to extrapolate one more time a new LJ parameter set that is again used for a QM/MM MD. This procedure of extrapolations was repeated five times as shown in Figure S4.

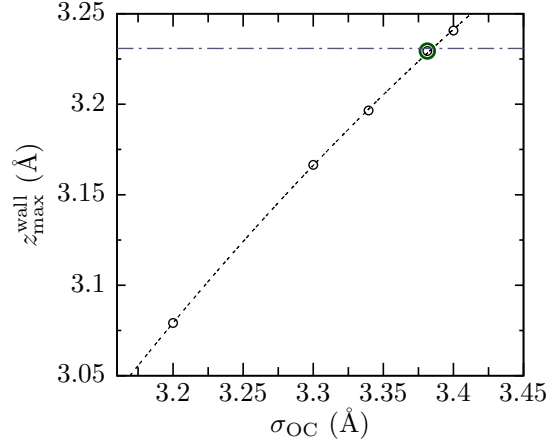


Figure S5. Position of the peak maximum of the density profile relative to the graphene walls ($z_{\text{max}}^{\text{wall}}$) for our previous L slit pore [6] as a function of the LJ parameter σ_{OC} using here QM/MM simulations as described in the text; see Table S2 for the other LJ parameters used in these simulations.

In order to improve the agreement, we take the best set and repeat the same approach using only σ_{OC} . This value is directly connected to the distance between the water molecules (oxygen atoms) and the wall (carbon atoms), thus with the position of the density maximum. We perform four more simulations varying the σ_{OC} parameter where the position of the maximum with respect to the wall ($z_{\text{max}}^{\text{wall}}$) is analyzed. With a simple second-order fitting analysis, the optimal σ_{OC} is obtained, see Figure S5. With this new parameter set reported in Table S2, the density profile fits correctly the height and the position of the maximum and, moreover, the water density profile across the entire slit pore is well represented overall. Most importantly, the resulting parameter set “LJ-QM/MM” is found to capture extremely well the RPBE-D3 reference density profile as obtained from full AIMD (i.e. all-QM) simulations for all slit pore widths, see Figure S6. We note in passing that this is different from what has been found previously for force field (all-MM) simulations where not a single set of LJ parameters could be optimized to represent the water stratification from XS to L slit pores. When using force field molecular dynamics, the only solution was to optimize different LJ parameter sets to describe the graphene-water interactions for the two smallest systems (namely XS and S) and all larger slit pores [6], see the LJ-S and LJ-L parameter sets in Table S2, respectively.

Table S2. Lennard-Jones parameter sets describing the graphene-water interactions optimized in this work for RPBE-D3 QM/MM simulations of all slit pore widths reported herein (LJ-QM/MM) and also the two previous sets optimized separately for force field (all-MM) simulations to describe all larger slit pores (LJ-L) and the monolayer and bilayer lamellae (LJ-S) from Ref. [6]; the parameters ε and σ are reported in units of kJ/mol and Å, respectively. Note that some misprinted data in this table have been corrected on 2023/12/20 while all simulations have been carried out using the correct data.

	σ_{CO}	ε_{CO}	σ_{CH}	ε_{CH}	
LJ-QM/MM	3.381	0.3172	2.300	0.1675	Present Work
LJ-L	3.308	0.3751	2.293	0.3119	Reference [6]
LJ-S	3.381	0.5384	2.084	1.5021	Reference [6]

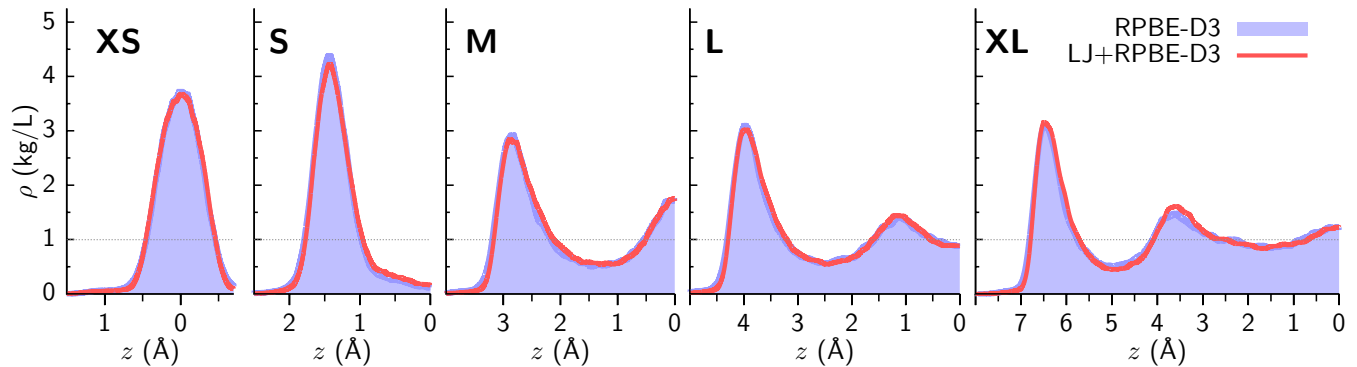


Figure S6. Water mass density profiles across the slit pores (i.e. along half of the z -axis being normal to the graphene sheets) for the systems XS to XL defined in Ref. 5 (from left to right) obtained therein with full AIMD (i.e. all-QM) reference simulations based on the RPBE-D3 density functional (shaded blue area) together with those obtained from the present QM/MM simulations thermostatted at 300 K (red lines) when using the new LJ-QM/MM parameterization for RPBE-D3 as reported in Table S2.

D. Pressure Control

1. Intrinsic Density Correction

Any water model, be it based on electronic structure theory or on parameterized force fields, has certain intrinsic properties which can differ from experiment. For example, the mass density of liquid water at 300 K and 1 bar of the SPC/E water model drops to $\approx 0.983 \text{ g/cm}^3$ after adapting [6] our force field setup for consistent use in narrow slit pores down to the monolayer limit (by not applying the usual long-range correction to the $-1/r^6$ dispersion interactions that is valid only in homogeneous three-dimensional systems), which now underestimates the experimental value ($\approx 0.996 \text{ g/cm}^3$). Much more serious deviations of the water density from experiment have been reported [21] when using GGA density functionals such as revPBE-D3 or BLYP-D2 resulting in under- and overestimation, respectively, in line with the present underestimation for RPBE-D3. Consequentially, we introduced in previous work [6] in the context of all-MM simulations the “intrinsic density correction” to correct for this systematic error in constant pressure simulations and, notably, in slit pore simulations with moving confining walls where constant normal (i.e. perpendicular) pressure is externally imposed; note that the density problem does not occur in constant volume simulations of bulk liquids in the NVT or NVE ensembles since the volume can be easily adjusted as to produce the correct experimental water density (at the desired thermodynamic P and T conditions given the number of water molecules in the periodic supercell). The intrinsic density correction consists in applying an excess in the simulated pressure (which could also be negative) to correct for this difference by increasing the density in constant pressure setups (as realized using the piston approach, see below, to control the normal pressure in water-filled graphene slit pores). For example, in the particular case of SPC/E, the pressure should be increased by 0.3 kbar (on top of the 1 bar ambient pressure which is completely negligible on the kilobar scale required for the density correction), to recover the proper experimental density [20] at ambient conditions (1 bar and 300 K) using the aforementioned slit pore setup [6]. Note that this correction is “automatically applied” in any standard NVT or NVE simulation of bulk liquids when the volume of the supercell is determined from the experimental density as customarily done in such constant volume simulations.

For RPBE-D3 water used in this work, see Section IIB for the setup details, we computed the intrinsic pressure generated by that density functional for water from the pressure tensor obtained from all-QM NVT simulations of bulk water at 300 K at different (fixed) water mass densities, see green symbols with green fitted line in Figure S7 and caption for simulation details. Given the experimental mass density versus hydrostatic pressure relation (see black symbols with black fitted line in Figure S7) one can see that RPBE-D3 density at 1 bar is severely underestimated (see left vertical dashed line), whereas the experimental density at 1 bar (see horizontal dotted line) is obtained at a hydrostatic pressure corresponding to 1.6 kbar (see right vertical dashed line). Thus, the correct experimental water density is obtained from all-QM RPBE-D3 simulations upon applying an excess pressure of 1.6 kbar (again the 1 bar ambient base pressure being an irrelevant offset), which provides the intrinsic density correction for that particular density functional. In order to cross-check the consistency of the density correction in our slit pore setups, we carried out rigid piston simulations (using the QM/MM approach to include the graphene sheets and a wide slit pore obtained using 350 water molecules to generate a bulk-like region at the center of the pore where the average water density can be determined), while applying constant normal pressures of 1.0, 1.6 and 3.0 kbar, see red symbols in Figure S7. The simulation at a normal pressure of 1.6 kbar is found to close to perfectly generate the experimental density of bulk

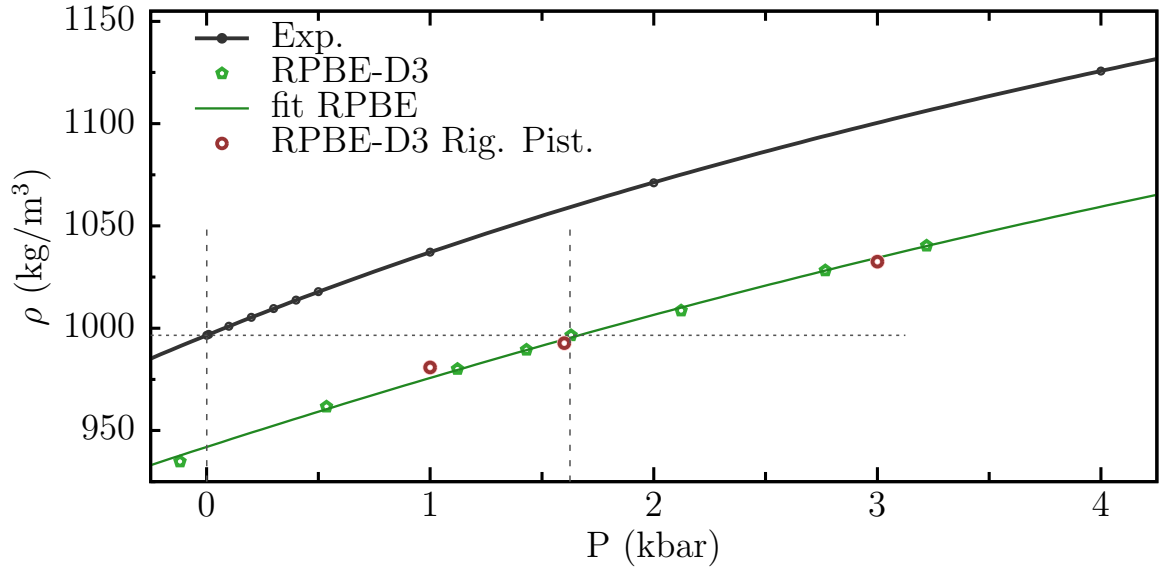


Figure S7. Bulk water mass density at 300 K as a function of pressure according to experiment [20] (black symbols with black fitted line) and obtained from RPBE-D3 simulations (present work) as follows: Green symbols (with green fitted line) are the pressures from the average stress tensor provided by all-QM NVT simulations of 200 ps duration after equilibration using 128 water molecules (at the corresponding densities ρ reported on the y -axis). Red symbols denote the average densities obtained from the bulk-like central region of a wide slit pore hosting 350 water molecules (between the same $a = 17.12$ Å and $b = 17.30$ Å graphene sheets as for all other slit pores treated) where a normal (perpendicular) piston pressure (corresponding to the pressure P reported on the x -axis) has been applied in rigid piston QM/MM simulations of 150 ps duration after equilibration. The dashed and dotted lines are used to extract the excess pressure of 1.6 kbar which compresses RPBE-D3 bulk water to the experimental density at 300 K and 1 bar; note that the rigid piston simulation at an applied pressure of 1.6 kbar exactly reproduces the experimental water density in the bulk-like central region of that wide slit pore. The computational setup is the same as described above.

water at 1 bar and 300 K in the central region of the slit pore, see horizontal dotted line, which validates our density correction approach when applied to slit pore setups. Thus, we always apply a normal excess pressure of 1.6 kbar in our rigid piston simulations at 300 K (as described in the next section) to account in all slit pores for the systematic underestimation of the water mass density by the RPBE-D3 functional.

2. Rigid Piston Simulations: Validation

Simulating anisotropic systems in general and very narrow slit pores in particular at controlled pressure conditions is not straightforward. For this reason, we introduced so-called “piston approaches” [6] which offer simple ways to control the normal (perpendicular) pressure in slit pore systems. This approach has been validated in our previous work at the level of using force field simulations, namely SPC/E water confined within graphene slit pores [6]. In our present work, we validate the rigid piston approach for QM/MM simulations where all water molecules (QM) are treated using the RPBE-D3 density functional while the confining two graphene walls (MM) interact with water via an adapted force field, see Section II C. Similarly to the previous force field work, we obtain the density at different normal pressures applied using the rigid piston approach in a large graphene-water slit pore that offers deep in its interior a bulk-like region with a volume that is large enough to compute the average water density therein. The QM/MM slit pore contains 350 H₂O between two graphene sheets consisting of 112 carbon atoms each (called XXL in our previous work [6]), which offers the same confining wall area as in the XS to L systems albeit in a wide slit pore. As the data in Figure S7 demonstrate, the bulk-like average water density ρ determined in that wide slit pore (red symbols) at constant rigid piston pressure P close to perfectly agrees with the average pressure P computed by averaging the stress tensor obtained in constant volume periodic bulk simulations at constant density ρ (green symbols and fitted line). Residual differences might be due to slower convergence of the rigid piston simulations since the piston exerts slow fluctuations of the graphene-to-graphene interlayer distance $d_{\text{int}}(t)$ at a given external pressure due to the dynamics of the two rigid graphene sheets.

3. Frozen Piston Simulations: Interlayer Distance Determination

We proposed previously three different ways to apply pistons in simulations of water in graphene-based slit pores, namely the flexible, rigid and frozen piston approaches [6]. In the first one, the graphene walls are not constrained at all except all carbon atoms being subject to an external normal force (i.e. perpendicular to the xy -plane of the slit pore defining the z -axis) that generates the external piston pressure, which implies that the two graphene sheets are internally fully flexible and thus can vibrate and buckle (a graphene force field based on RPBE-D3 has also been parameterized previously in Ref. 6). In the rigid piston treatment, all carbon atoms of the respective graphene wall are restrained to be in the same plane and kept there in their perfect crystallographic xy -positions, implying that the two rigid planes can move along the z -axis but without any internal deformation from coplanarity. Finally, in the frozen piston approach used here to compute statistically converged THz spectra, all carbon atoms are frozen in three-dimensional space, meaning that the interlayer distance cannot change. This implies that the constant graphene-to-graphene distance d_{int} must be determined beforehand as to set the desired pressure in frozen piston simulations.

Following our validated protocol to determine that interlayer distance [6], we carried out rigid piston simulations for each slit pore setup XS to L with the suitable number of water molecules (see Table S1) at the desired ambient pressure of 1 bar (thus applying the excess pressure of 1.6 kbar to establish the intrinsic RPBE-D3 density correction as described in Section IID 1) while simultaneously thermostating at 300 K. This allows us to compute the average interlayer distance between the two coplanar graphene sheets which provides the fixed interlayer distances d_{int} as reported in Table S1 for the present XS to L QM/MM slit pore setups. The initial positions and velocities for the rigid piston simulations were generated by pre-equilibration using all-MM simulations of 1 ns duration that employ the tailor-made force field setup from our previous work [6]. These initial conditions serve as input for the subsequent four independent rigid piston simulations. The running averages of the interlayer distances of the four slit pore setups obtained from these simulations are depicted in Figure S8 where the first 5 ps have been discarded from the averaging based on previous experience [6]. The final averages of the four interlayer distances (as reported Table S1) are taken to be the values at the end of the shown rigid piston simulations and used to run frozen piston simulations in the NVT ensemble and subsequently in the NVE ensemble. All reported THz spectra have been obtained from the latter microcanonical RPBE-D3 QM/MM NVE-simulations by averaging over 60 independent NVE trajectories for the XS, S, M, and L slit pore setups generated from frozen piston RPBE-D3 QM/MM NVT simulations as detailed in Section IIB.

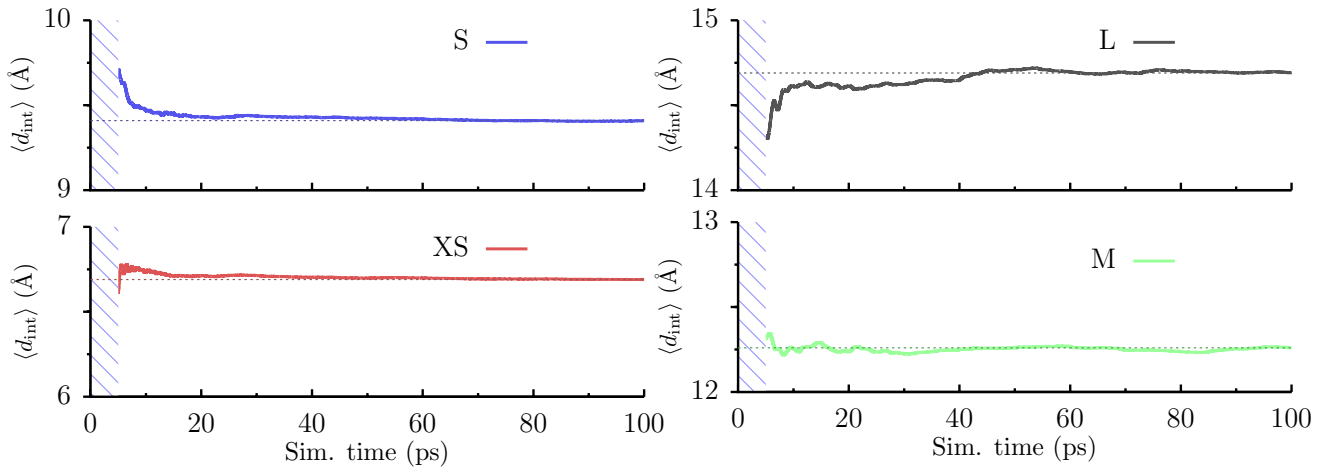


Figure S8. Running average of the interlayer distance between the two coplanar graphene sheets for the four different slit pore setups investigated in the present work (namely XS, S, M, and L as defined in Section II A) obtained from rigid piston RPBE-D3 NVT simulations thermostatted to 300 K and applying an excess pressure of 1.6 kbar to establish experimental 1 bar conditions as explained in the text. The first 5 ps (dashed areas) are discarded from averaging and the values at 100 ps are used to determine the average interlayer distance that is fixed at d_{int} (compiled in Table S1) in the frozen piston simulations used to compute the THz spectra.

III. DISSECTION OF THEORETICAL THZ SPECTRA

A. Polarization-resolved Spectra

The IR/THz absorption spectrum is computed via the Fourier transform (\mathcal{F}) of the time correlation function of the total dipole moment derivative ($\dot{\mathbf{M}}$),

$$\alpha(\omega) n(\omega) = S(\omega) = \frac{\beta}{6cV\epsilon_0} \mathcal{F} [\langle \dot{\mathbf{M}}(0)\dot{\mathbf{M}}(t) \rangle] \quad , \quad (3.1)$$

where $\beta = 1/k_B T$, T is the temperature, c the speed of light in vacuum, V the volume, ϵ_0 the vacuum permittivity and $n(\omega)$ the frequency dependent refractive index. The total dipole moment of the confined water lamellae,

$$\mathbf{M}(t) = \sum_i^{N_{\text{nuclei}}} q_i \mathbf{r}_i(t) - 2 \sum_j^{N_{\text{wanniers}}} \mathbf{r}_j(t) \quad , \quad (3.2)$$

is defined using the positions and charges of all maximally localized Wannier centers [11] associated to the water molecules and those of all oxygen and hydrogen nuclei in the simulation box. Note that we exclusively deal with paired electrons in our system, therefore the charge of each Wannier orbital equals -2 which is assigned to its center at position $\mathbf{r}_j(t)$. Also note that pseudopotentials are used, thus only the Wannier orbitals of the valence electrons are considered in the second sum and, thus, q_i are the pseudocharges of the nuclei where the core electrons included in the pseudopotential are considered. We employ finite differences to compute the total dipole moment time derivative as before [22]. The frequency-dependent refractive index $n(\omega)$ can in principle be computed from the calculated spectra via the Kramers-Kronig relations [22, 23]. However, its application requires to know n in the optical gap between the vibrational excitations and the lowest electronic excitation which is well known for bulk water but, unfortunately, unknown for the investigated slit pore systems. We therefore restrict ourselves to the discussion of $S(\omega) = \alpha(\omega) n(\omega)$ as defined in Eq. (3.1).

Since confined water in slit pores is not isotropic as the walls impose a xy -plane parallel to the frozen coplanar graphene sheets and the corresponding normal z -axis perpendicular to them, it is useful to decompose the THz spectrum in terms of the corresponding polarization directions. This can be realized by expanding the dot product in Eq. (3.1),

$$S(\omega) = \sum_i^3 S_i(\omega) = \frac{\beta}{6cV\epsilon_0} \mathcal{F} \left[\sum_i^3 \langle \dot{M}_i(0)\dot{M}_i(t) \rangle \right] \quad , \quad (3.3)$$

where $\dot{M}_i(t)$ denotes the i -th Cartesian component of the total dipole moment derivative vector $\dot{\mathbf{M}}(t)$ at time t . In our system setup, the z -component is perpendicular to the graphene planes while the x - and y -components together define these planes. Therefore, the spectra in the xy -plane, $S_{xy}(\omega) = S_x(\omega) + S_y(\omega)$, and along the z -axis, $S_z(\omega)$, provide information about the anisotropy of the IR/THz response of water in these slits pores. The polarization-resolved THz spectra are individually analyzed in the Main Text.

B. Cross-correlation Analysis

The Cross Correlation Analysis (CCA) was originally introduced [19] to dissect THz spectra of aqueous electrolyte solutions of simple ions into individual spectral contributions from the ion itself, first shell, and second shell water molecules as well as from the couplings between these classes. Within the CCA, the THz spectrum is mathematically exactly split into individual contributions, i.e. when adding up all of them the full THz spectrum is exactly recovered. Therefore, no intensity is artificially added or removed from the total IR/THz spectrum as a result of its CCA decomposition. Using this analysis tool, we could already successfully dissect the THz response of complex molecular solutes in water such as the amino acids glycine and valine [24] as well as of ions in finite microsolvating water clusters [25]. Moreover, we provided a general equation [19] which allows one to rigorously decompose total IR/THz spectra in terms of any topological group of molecules or even molecular fragments which are spectroscopically meaningful to describe the system. That way it was possible to dissect the THz spectrum of aqueous glycine and valine solutions [24] and therein distinguish the spectral response of ‘‘hydrophilic’’ and ‘‘hydrophobic’’ water molecules.

The basis of the CCA method are molecular dipole moments $\boldsymbol{\mu}_i$ which can be computed in the very same way as the total dipole moment Eq. (3.2), but only considering the nuclei and Wannier centers belonging to a single molecule i . Since the total dipole moment is exactly the sum of all molecular dipole moments, the absorption coefficient in Eq. (3.1) can be expressed equivalently as a sum of individual molecular contributions,

$$S(\omega) = \frac{\beta}{6cV\epsilon_0} \mathcal{F} \left[\sum_{ij}^{N_{\text{mol}}} \langle \dot{\boldsymbol{\mu}}_i(0)\dot{\boldsymbol{\mu}}_j(t) \rangle \right] \quad , \quad (3.4)$$

where the double sum runs over all N_{mol} molecules in the slit pore systems thus yielding N_{mol}^2 distinct spectral contributions in total. In the spirit of the CCA technique, the individual molecular spectral contributions can be exactly split into all interactions between two molecules (cross-correlations or “cross terms”) and the contributions of all individual molecules (auto-correlations or “self terms”),

$$S(\omega) = S^{\text{A}}(\omega) + S^{\text{C}}(\omega) = \frac{\beta}{6cV\epsilon_0} \mathcal{F} \left[\sum_i^{N_{\text{mol}}} \langle \dot{\boldsymbol{\mu}}_i(0) \dot{\boldsymbol{\mu}}_i(t) \rangle \right] + \frac{\beta}{6cV\epsilon_0} \mathcal{F} \left[\sum_{i \neq j}^{N_{\text{mol}}} \langle \dot{\boldsymbol{\mu}}_i(0) \dot{\boldsymbol{\mu}}_j(t) \rangle \right], \quad (3.5)$$

where we introduce the shorthand notations “**A**” and “**C**” that are used in the Main Text to denote the corresponding $S^{\text{A}}(\omega)$ and $S^{\text{C}}(\omega)$ spectra, respectively. Cross correlations can be negative and thus their interpretation is more involved compared to auto-correlations, which are strictly positive. We note again that the definition of molecular dipole moments used within the CCA is very general and not restricted to entire water molecules only, but can be extended to fragments such as functional groups of sufficiently large molecules [24].

Depending on N_{mol} , the analysis of all N_{mol} auto and $N_{\text{mol}}(N_{\text{mol}} - 1)$ cross terms is not only a tedious task, but only of very limited use since way too much information is provided that way. The basic idea of the CCA method is now to group molecules together based on topological criteria, e.g. grouping together all water molecules that are in the first solvation layer close to graphene walls in the present case. By introducing such groups, the number of spectral terms in Eq. (3.4) is greatly and meaningfully reduced which allows one to interpret the obtained spectral contributions in a topological context that is adapted to the problem of interest, e.g. the possibly distinct spectral responses of water molecules in the interfacial (IF) and intermediate (IM) layers and their putative couplings (see Main Text). Notably, molecules are dynamic entities and, thus, they might change their group membership over time. This happens, for example, when a water molecule leaves the first solvation layer of a graphene wall by diffusion toward the interior of the water lamella. Such molecules contribute to the so-called “exchange terms”.

Putting all these pieces together, the information on all defined topological groups is incorporated in the most general CCA expression which yields the spectral contributions

$$S_{\zeta\xi}^{\gamma}(\omega) = \frac{\beta}{6cV\epsilon_0} \mathcal{F} \left[C_{\zeta\xi}^{\gamma}(t) \right] \quad (3.6)$$

due to the self, cross and exchange terms involving those groups, where $C_{\zeta\xi}^{\gamma}(t)$ is the time correlation function of all molecule pairs which belong to the topological groups ζ and ξ . We refer the interested reader to the Supporting Information of Ref. 19 for a complete mathematical derivation of $C_{\zeta\xi}^{\gamma}(t)$. Note that γ allows one to introduce so-called “relations” between molecules, which can for instance be H-bonded versus non H-bonded water pairs to split cross-correlations even further as elaborated in Ref. 19. In the present manuscript, we do not divide cross-correlations any further such that we are left with spectra due to auto- and cross-correlations, $S^{\text{A}}(\omega)$ and $S^{\text{C}}(\omega)$ respectively, as explicitly shown in Eq. (3.5). While Eq. (3.6) seems to be complicated at first glance, the definition and its application are quite straightforward which will become clear in the following two subsections.

C. Orientational Decomposition

The orientation of the water molecule adjacent to the graphene sheet, i.e. in the IF water layers, can be quantified using the angle β as previously introduced [26] and illustrated in Fig. S9. For a given water molecule in a slit pore, β is defined to be the angle between the graphene plane (xy) and the vector normal to the plane that is defined by the three atoms of that water molecule. The angle β ranges from 0 to 90° , where 90° means that the molecule is oriented parallel to the xy -plane, while 0° corresponds to a fully perpendicular arrangement.

In case of a fully random orientation, the cosine of β must be uniformly distributed, being not the case in the investigated systems (see Fig. S10 where the solid black lines correspond to the random orientation). For instance, in case of the bilayer system S, there is clear preference for water molecules being oriented either parallel (in-plane) or perpendicular (normal) to the surface. In the latter case, one OH group vector points away from the graphene plane, which is why we call this an “out-of-plane” configuration. Using the CCA technique, we now dissect the THz spectra of the water lamellae in terms of contributions stemming from the in-plane ($\beta > 45^\circ$, symbol \parallel) and from the out-of-plane ($\beta < 45^\circ$, symbol \perp) water molecules; using 45° is selected after inspecting the distribution functions of β in Fig. S10. This definition in terms of \parallel and \perp water molecule orientations within the slit pores yields three distinct self term contributions $S^{\text{A}}(\omega)$ to the total THz spectrum, namely $S_{\parallel\parallel}^{\text{A}}(\omega)$, $S_{\parallel\perp}^{\text{A}}(\omega)$ and $S_{\perp\perp}^{\text{A}}(\omega)$ computed from Eq. (3.6). In the Main Text, we use the more intuitive shorthand notations $\mathbf{A}\parallel$, $\mathbf{A}\parallel\rightleftharpoons\perp$ and $\mathbf{A}\perp$, respectively. The first and third contribution contain the spectral self term of in-plane and out-of-plane water molecules, respectively. The second term is the exchange term stemming from water molecules which change their orientation along the trajectory from an in-plane to an out-of-plane configuration or vice versa.

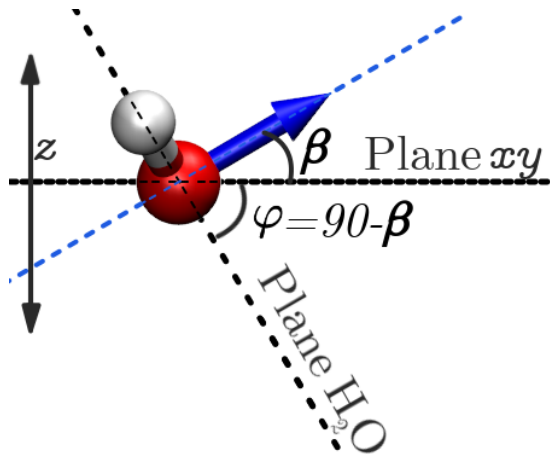


Figure S9. Definition of the β angle of a water molecule within a slit pore, where the xy -plane is indicated by a dashed line, the intramolecular water plane is marked as a black dotted line and the normal to the water plane is marked as a blue dotted line with arrow.

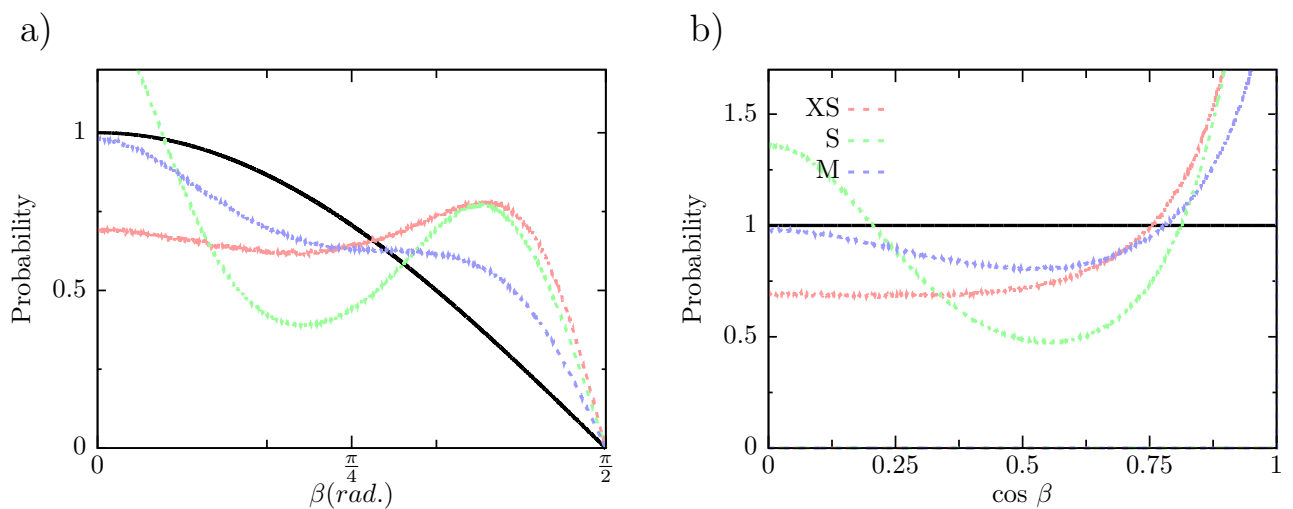


Figure S10. Probability distribution functions of β and $\cos \beta$ in the left and right panels, respectively, of the orientations of the water molecules in the XS, S and M slit pores where β is defined in Figure S9.

D. Layer-wise Decomposition

In case of the monolayer (XS) and bilayer (S) systems, there are only one and two layers of water molecules, respectively, meaning that all water molecules are adjacent to a graphene sheet and, thus, are interfacial (IF) water molecules. For the larger multilayer systems M and L, however, there are water molecules in intermediate (IM) layers which are not directly adjacent to a graphene sheet but surrounded by other water molecules as illustrated in Figure 1 of the Main Text. It is expected that water molecules in the first solvation layer of the graphene walls behave differently compared to water molecules which are exclusively surrounded by other water molecules. Therefore, we introduce yet another system-adapted CCA decomposition to dissect the THz spectrum depending on the location of the water molecules within the different slit pores. Topologically, layers can straightforwardly be defined by the density minima across the slit pores, i.e. along the z -axis perpendicular to the graphene sheet as shown in Figure 1 of the Main Text, thus providing the IF and IM layers which contain IF and IM water molecules.

Defining now a CCA splitting using the IF and IM layer definition yields three important contributions which are necessary to understand the THz spectra due to water lamellae in the different slit pores, namely $S_{\text{IF IM}}^{\text{C}}(\omega)$, $S_{\text{IF IF}}^{\text{C}}(\omega)$, and $S_{\text{IM IM}}^{\text{C}}(\omega)$ where we introduce again respective shorthand notations **C** IF-IM, **C** IF-IF and **C** IM-IM in the Main Text. The first term describes the spectral contribution stemming from cross-correlations between two water molecules where one is in the IF and the other in the IM layer, i.e. this term mainly contains exclusively *interlayer* water pairs. The latter two terms describe cross-correlations between two water molecules with are both in an IF or IM layer, respectively, i.e. these spectral contributions are due to *intralayer* water pairs.

IV. SUPPORTING COMPUTATIONAL ANALYSES

A. Full-range IR spectra

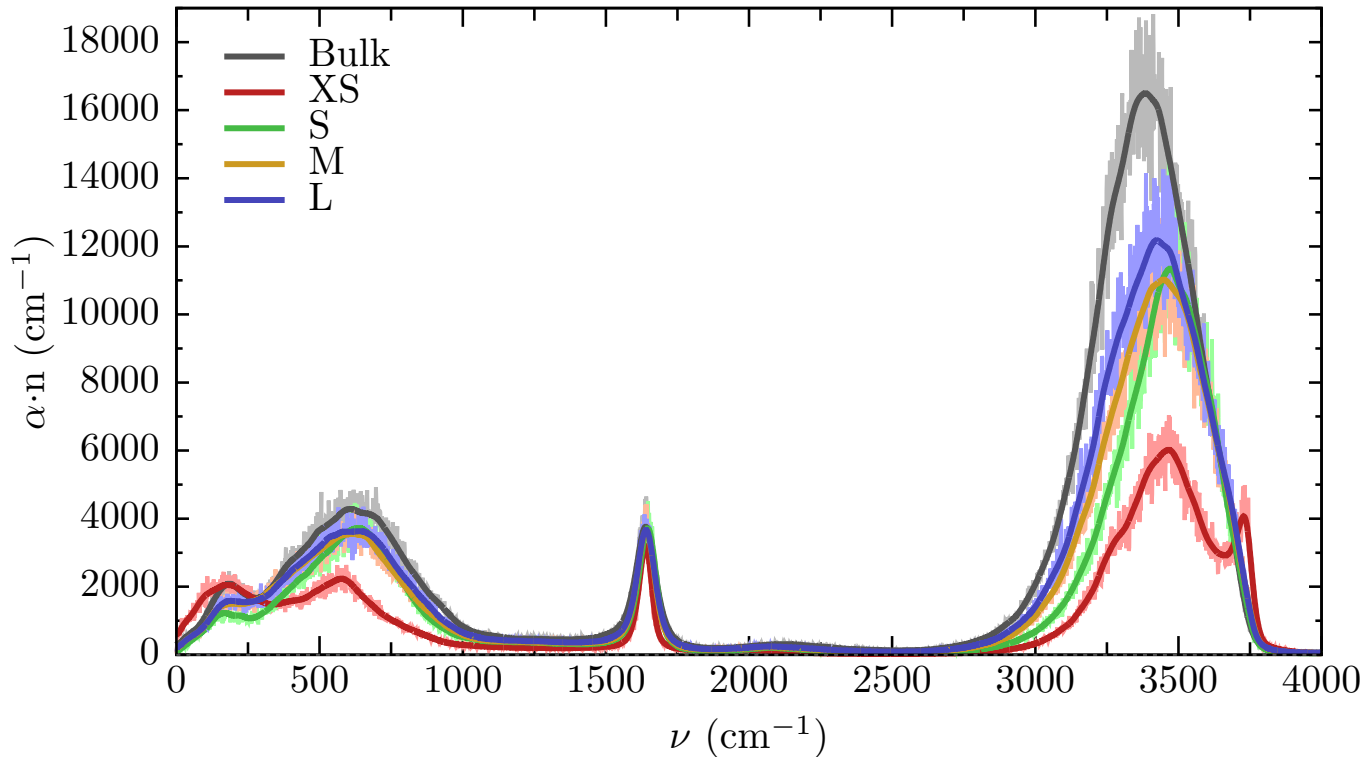


Figure S11. Theoretical IR spectra of water confined in the XS, S, M, and L graphene slit pore systems as defined in Section II A compared to bulk water at ambient conditions (300 K and 1 bar). The effective volume V required in the normalizing prefactor according to Eq. (3.1) has been adjusted such that the maximum of the intramolecular bending mode of water confined in the individual slit pore systems matches that of bulk water at $\approx 1640 \text{ cm}^{-1}$.

B. Vibrational Density of States (VDOS)

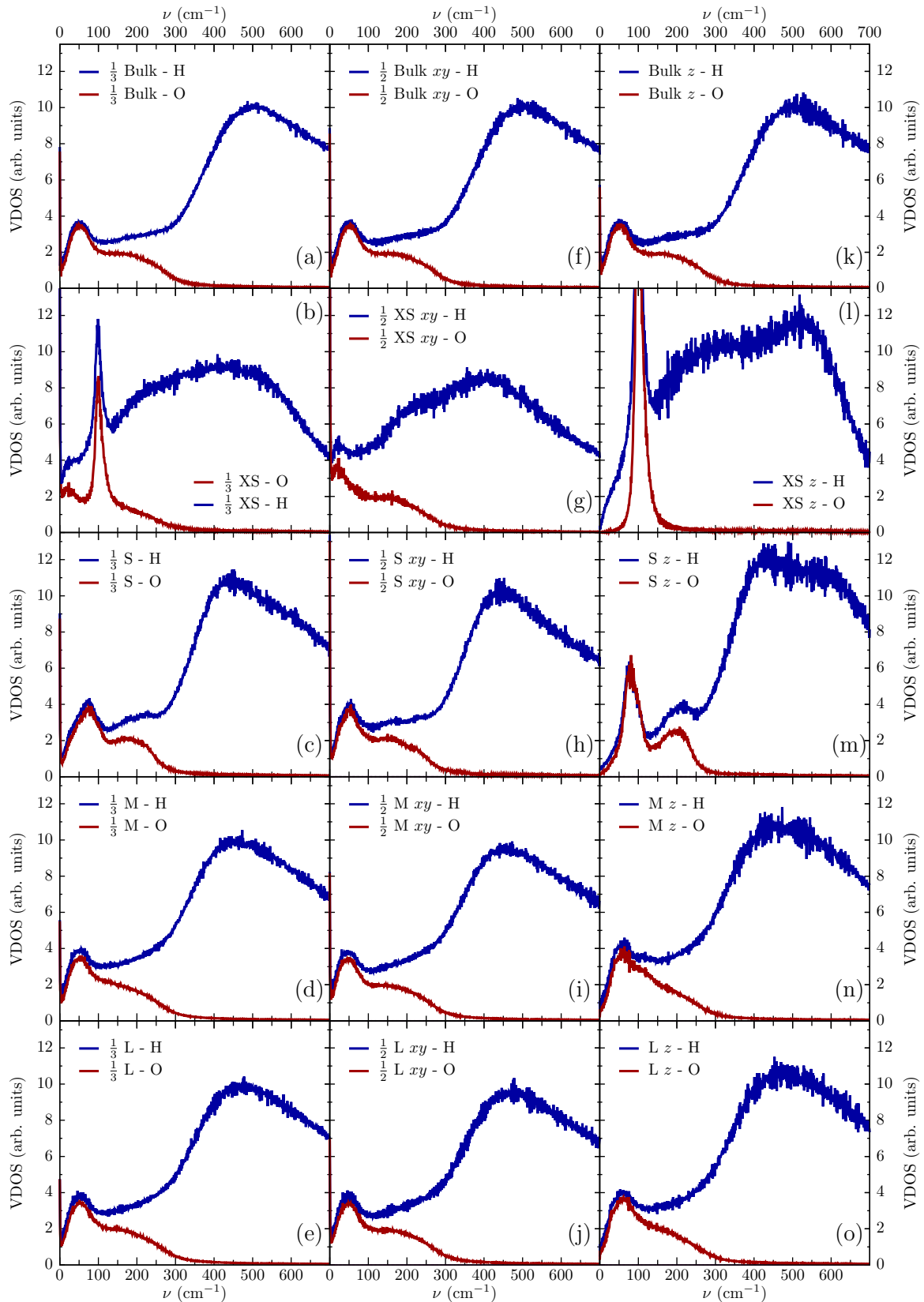


Figure S12. Oxygen and hydrogen VDOS for bulk water at ambient conditions (panels a, f and k) and of water confined in the four different graphene-water slit pores: monolayer system XS (panels b, g and l), bilayer system S (panels c, h and m), trilayer system M (panels d, i and n), and four-layer system L (panels e, j and o) as defined in Section II A. The first column reports the total spectra (a-e), the second the xy -components (f-j) and the last one the z -components (k-o); note that the splitting into the latter components is of a purely formal nature for isotropic bulk water. All spectra have been scaled by using the factor that sets the maximum of the H-VDOS for bulk water to 10.

C. Two-body Vibrational Density of States (2B-VDOS)

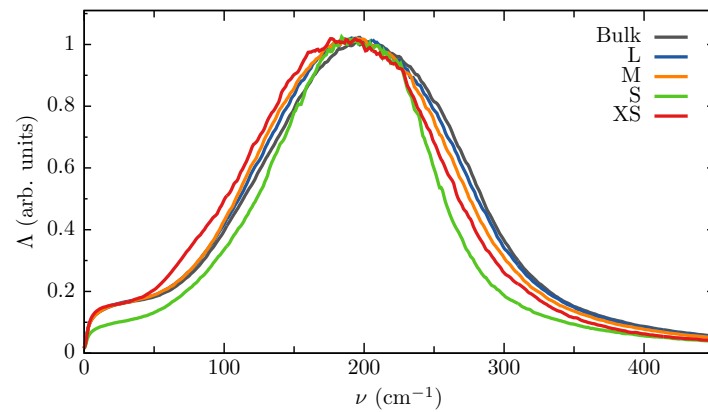


Figure S13. Two-body vibrational density of states (as introduced in Eqs. (1) and (2) of Ref. 27) of water confined in the four different slit pore systems in direct comparison to bulk water at ambient conditions; the maximum intensities have been scaled to unity.

D. M Slit Pore System: Spectral Decompositions

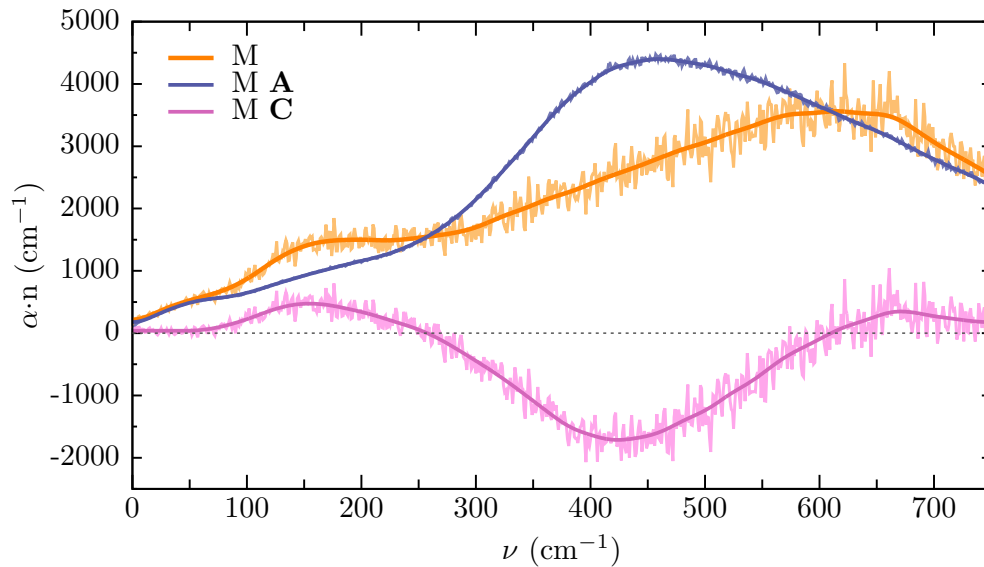


Figure S14. Theoretical THz spectrum of trilayer water in the M graphene slit pore (M) and its decomposition into the auto-correlation (M A) and cross-correlation (M C) terms; see Main Text for the same decomposition of the XS, S, and L systems.

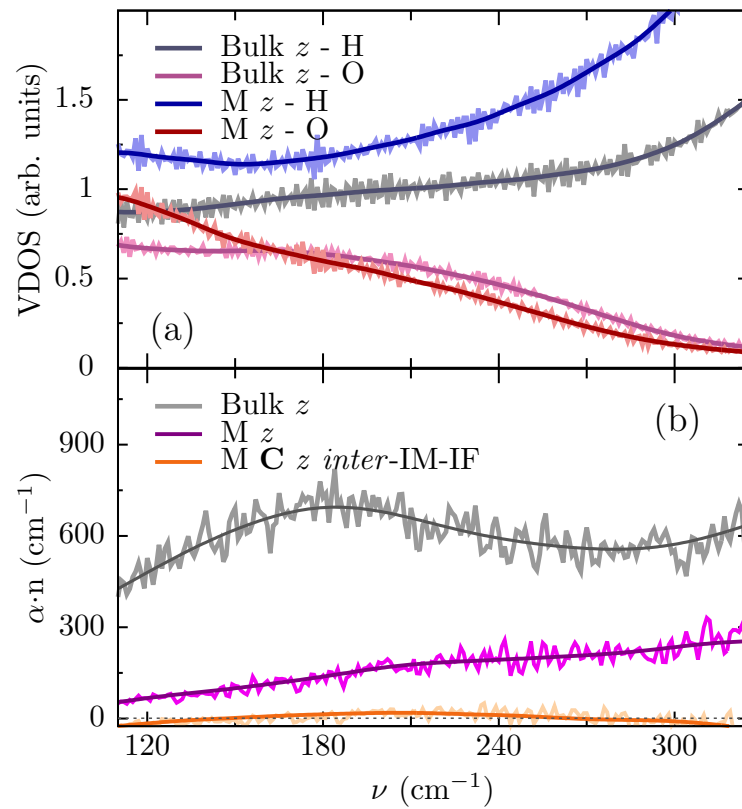


Figure S15. Polarization-resolved VDOS and THz spectra of nanoconfined water in the M graphene slit pore perpendicular to the graphene walls: (a) z -polarized O-VDOS and H-VDOS spectra of bulk water (Bulk) and trilayer water (M); (b) z -polarized THz spectrum of slit pore M and the corresponding cross-correlation contributions due to water pairs where one molecule is in an interfacial layer and the other one in the intermediate layer (\mathbf{C} *inter-IF-IM*); see Main Text for similar decompositions of the S and L systems.

-
- [1] R. Nair, H. Wu, P. Jayaram, I. Grigorieva and A. Geim, *Science*, 2012, **335**, 442–444.
- [2] N. Wei, X. Peng and Z. Xu, *ACS Appl. Mater. Interfaces*, 2014, **6**, 5877–5883.
- [3] G. Schwaab, F. Sebastiani and M. Havenith, *Angew. Chem. Int. Ed.*, 2019, **58**, 3000–3013.
- [4] F. Sebastiani, A. V. Verde, M. Heyden, G. Schwaab and M. Havenith, *Phys. Chem. Chem. Phys.*, 2020, **22**, 12140–12153.
- [5] S. Ruiz-Barragan, D. Muñoz-Santiburcio and D. Marx, *J. Phys. Chem. Lett.*, 2019, **10**, 329–334.
- [6] S. Ruiz-Barragan, D. Muñoz-Santiburcio, S. Körning and D. Marx, *Phys. Chem. Chem. Phys.*, 2020, **22**, 10833–10837.
- [7] *CP2K Open Source Molecular Dynamics*, <https://www.cp2k.org/>.
- [8] J. VandeVondele, M. Krack, F. Mohamed, M. Parrinello, T. Chassaing and J. Hutter, *Comput. Phys. Commun.*, 2005, **167**, 103–128.
- [9] J. Hutter, M. Iannuzzi, F. Schiffmann and J. VandeVondele, *Wiley Interdiscip. Rev. Comput. Mol. Sci.*, 2014, **4**, 15–25.
- [10] T. D. Kühne, M. Iannuzzi, M. Del Ben, V. V. Rybkin, P. Seewald, F. Stein, T. Laino, R. Z. Khaliullin, O. Schütt, F. Schiffmann, D. Golze, J. Wilhelm, S. Chulkov, M. H. Bani-Hashemian, V. Weber, U. Borstnik, M. Taillefumier, A. S. Jakobovits, A. Lazzaro, H. Pabst, T. Müller, R. Schade, M. Guidon, S. Andermatt, N. Holmberg, G. K. Schenter, A. Hehn, A. Bussy, F. Belleflamme, G. Tabacchi, A. Glöß, M. Lass, I. Bethune, C. J. Mundy, C. Plessl, M. Watkins, J. VandeVondele, M. Krack and J. Hutter, *J. Chem. Phys.*, 2020, **152**, 194103.
- [11] D. Marx and J. Hutter, *Ab Initio Molecular Dynamics: Basic Theory and Advanced Methods*, Cambridge University Press, Cambridge, 2009.
- [12] B. Hammer, L. B. Hansen and J. K. Nørskov, *Phys. Rev. B*, 1999, **59**, 7413–7421.
- [13] S. Grimme, J. Antony, S. Ehrlich and H. Krieg, *J. Chem. Phys.*, 2010, **132**, 154104.
- [14] S. Goedecker, M. Teter and J. Hutter, *Phys. Rev. B*, 1996, **54**, 1703.
- [15] C. Hartwigsen, S. Goedecker and J. Hutter, *Phys. Rev. B*, 1998, **58**, 3641.
- [16] M. Krack, *Theor. Chem. Acc.*, 2005, **114**, 145–152.
- [17] J. G. Brandenburg, A. Zen, D. Alfè and A. Michaelides, *J. Chem. Phys.*, 2019, **151**, 164702.
- [18] M. Heyden, J. Sun, S. Funkner, G. Mathias, H. Forbert, M. Havenith and D. Marx, *Proc. Natl. Acad. Sci. U.S.A.*, 2010, **107**, 12068–12073.
- [19] P. Schienbein, G. Schwaab, H. Forbert, M. Havenith and D. Marx, *J. Phys. Chem. Lett.*, 2017, **8**, 2373–2380.
- [20] W. Wagner and A. Pruß, *J. Phys. Chem. Ref. Data*, 2002, **31**, 387–535.
- [21] M. Galib, T. T. Duignan, Y. Misteli, M. D. Baer, G. K. Schenter, J. Hutter and C. J. Mundy, *J. Chem. Phys.*, 2017, **146**, 244501.
- [22] M. Smiechowski, J. Sun, H. Forbert and D. Marx, *Phys. Chem. Chem. Phys.*, 2015, **17**, 8323–8329.
- [23] R. Iftimie and M. E. Tuckerman, *J. Chem. Phys.*, 2005, **122**, 214508.
- [24] A. Esser, H. Forbert, F. Sebastiani, G. Schwaab, M. Havenith and D. Marx, *J. Phys. Chem. B*, 2018, **122**, 1453–1459.
- [25] P. K. Gupta, P. Schienbein, J. Daru and D. Marx, *J. Phys. Chem. Lett.*, 2019, **10**, 393–398.
- [26] U. Terranova and N. H. de Leeuw, *J. Chem. Phys.*, 2016, **144**, 094706.
- [27] P. Schienbein and D. Marx, *Angew. Chem. Int. Ed.*, 2020, **59**, 18578–18585.